IEEE Access
Multidisciplinary | Rapid Review | Open Access Journal

Received 14 September 2022, accepted 4 October 2022, date of publication 10 October 2022, date of current version 25 October 2022.

Digital Object Identifier 10.1109/ACCESS.2022.3213690

RESEARCH ARTICLE

Numerical and Experimental Investigations on Influence of Internal Defect Parameters on Partial Discharge Induced UHF Signals in Gas Insulated Switchgear

YUGANDHARA RAO YADAM[1], RAMANUJAM SARATHI[2], (Senior Member, IEEE), AND KAVITHA ARUNACHALAM[1], (Senior Member, IEEE)

[1]Department of Engineering Design, Indian Institute of Technology Madras, Chennai 600036, India
[2]Department of Electrical Engineering, Indian Institute of Technology Madras, Chennai 600036, India

Corresponding author: Kavitha Arunachalam (akavitha@iitm.ac.in)

This work was supported by the Central Power Research Institute (CPRI), India, under Grant CPRI/R&D/TANS/2019.

ABSTRACT A detailed study of the influence of internal defect parameters on partial discharge (PD) induced ultrahigh frequency (UHF) signals propagated through an L section of metal encapsulated gas insulated switchgear (GIS) is presented. The study is carried out using PD defect model with varying rise time, defect size, location, and orientation, an ultrawideband UHF internal sensor, and 3 m long L-GIS with dielectric spacers, shorting plates, hand holes and bus bar with disconnector. Presence of higher order modes, multipath propagation, losses, and dispersion inside L-GIS were observed to influence the time and frequency domain characteristics of PD signals induced in the internal UHF sensor with 0.5 to 6.8 GHz operating bandwidth and directional radiation pattern. The rise time of PD signals significantly influenced UHF signal characteristics in time and frequency domains while PD defect size, location and angular orientation primarily affected the signal amplitude. UHF sensor measurements confirmed the complex behavior of PD induced electromagnetic wave propagation inside L-GIS for varying defect parameters in agreement with the simulations. Despite the complex behavior, it is concluded that PD sensing in GIS is possible using ultrawideband internal UHF sensor.

INDEX TERMS Gas insulated switchgear, partial discharge, protrusion defect, ultrahigh frequency.

I. INTRODUCTION

Partial discharge (PD) detection using ultrahigh frequency (UHF) method has been widely investigated for condition monitoring of power apparatus due to its high sensitivity, immunity to external noise and ability to detect variety of PD activity [1], [2], [3], [4], [5], identify defect type [6], [7], locate the source [2] and assess the insulation condition in high voltage (HV) equipment [8]. UHF PD sensing is gaining acceptance for condition monitoring of ageing gas insulated switchgear (GIS) [9], [10], [11], [12]. GIS is a metal encapsulated power equipment consisting of several HV components. The changing dimensions of GIS due to the internal components, electrical discontinuities, and branching result in complex electromagnetic (EM) wave behavior inside the GIS and influence the propagation path and characteristics of PD induced UHF signals [11], [13], [14], [15], [16], [17], [18], [19].

Due to the complex construction, understanding the characteristics of PD induced UHF signals inside the GIS helps to determine the PD detection capability of UHF sensor and UHF sensor placement inside the GIS prior to field testing. Though not a perfect coaxial line, the coaxial arrangement of the HV conductor inside the metal encapsulation supports the fundamental transverse EM (TEM) mode, as well as higher order transverse electric (TE) and transverse magnetic (TM)

The associate editor coordinating the review of this manuscript and approving it for publication was Pavlos I. Lazaridis.

modes. Okabe et al. studied the EM signal characteristics in L and T sections of GIS using time domain simulations [13], [18]. Kaneko et al. extended the simulation work in [15] and reported that EM signal strength varied in L and T GIS sections. These numerical studies did not include insulating spacers, PD defects, hand holes, disconnector, internal UHF sensors and shorting plates which significantly influence UHF signal propagation and their characteristics. Hoshino et al. simulated a GIS bus bar in time domain with three dielectric spacers, and reported that EM wave attenuation by the insulating spacer was 10–35% but did not report modal analysis or measurements [16]. Hikita et al. experimentally investigated the influence of spacer on PD signal strength in a straight GIS with four spacers, and observed up to 30% reduction in signal amplitude [20]. The insulating spacers create discontinuity in the external metal encapsulation. As a result, part of the PD induced UHF signal leaks out of the GIS and weak EM emissions could also be detected by an external UHF sensor [21]. As the signal strength of the leaked EM wave is relatively weak [16], internal UHF sensors are widely investigated for PD detection in GIS [22], [23], [24], [25], [26]. Wang et al. studied the propagation characteristics of PD induced UHF signals in simple straight and L-GIS for a protrusion defect using time domain simulations and numerical probes [27], [28]. Numerical probes yield optimistic results as they have isotropic and broadband behaviour unlike practical internal UHF antenna. Darwish et al. studied the influence of disconnecting switches on PD induced UHF signals inside a L-GIS with spacers and handholes using an artificial internal transmitter connected to a wideband signal generator to inject PD-like signals [11].

Existing studies on UHF signal propagation in GIS are mostly numerical investigations in varying GIS geometry [11], [15], [17], [18], [29], [30], defect location [27], [28], [31], [32] and UHF orientation [11], [27], [32]. A significant number of them are simulations and only a few provide insights on EM wave propagation [11], [27], [30]. Experimental study of PD activity in GIS test cells using commercial UHF disc sensor indicated that the UHF signal bandwidth varied depending on the PD defect type [33]. Based on our earlier work, we developed a 150 mm diameter ultrawideband conical monopole antenna (CMA) with protective radome, operating bandwidth of 0.5−6.8 GHz and mean effective height of 19.4 mm for PD sensing [25]. PD signals gathered by the UHF CMA for Corona, particle movement and surface discharge activity in GIS test cells indicated about two-fold increase in the induced voltage when compared to commercial disc sensor [25]. Existing studies did not analyse the influence of PD signal rise time i.e., defect type and defect size on UHF signals propagating inside the GIS. Furthermore, detailed numerical simulations and experimental verification using a practical ultrawideband UHF sensor has not been reported as well.

In this work, we present a detailed study of UHF signal propagation characteristics in L-GIS with dielectric spacers, shorting plates, hand holes and bus bar with disconnector for PD defect of varying bandwidth i.e., rise time and size using our ultrawideband CMA as the internal PD sensor. Transient and steady state simulations were experimentally verified in a laboratory L-GIS setup. Numerical and experimental techniques adopted were used to verify the influence of defect location and orientation on UHF signals propagated inside L-GIS reported in literature. Thus, PD detection capability and sensitivity of the internal UHF CMA was assessed for varying defect parameters in a L-GIS setup with geometrical and material discontinuities using an internal transmitter injecting PD-like signals prior to testing in a HV GIS equipment.

The organization of this work is as follows: Numerical modelling of L-GIS, internal CMA sensor, and PD defect and EM simulations carried out for understanding UHF signal propagation and reception by the internal UHF sensor are presented in Section II. Laboratory setup and measurements carried out for experimental verification are presented in Section III. Detailed discussion of simulation and measurement results for varying PD defect parameters are presented in Section IV followed by conclusion in Section V.

II. NUMERICAL MODELING

A. GIS MODEL

Fig. 1 shows the 3D model of 3 m long L-GIS used in this study. The structure is a coaxial transmission line consisting of three straight sections (S_1, S_2, S_3), one right-angled L section (L_1) and two shorting plates at the ends as shown in Fig. 1. The inner (r_i) and outer (r_0) radii of the GIS are 60 and 200 mm, respectively based on a 252 kV GIS model [27]. The dielectric medium inside the GIS was assigned as SF_6 gas with dielectric constant 1.00205 [27]. Three tapered basin type insulating spacers (I_1, I_2 and I_3) of 70 mm thickness and 500 mm outer diameter were used in the L-GIS.

B. INTERNAL UHF SENSOR

The CMA with ultrawide operating bandwidth reported in our earlier work was used as the internal UHF sensor (Fig. 2) [25]. Fig. 2(a) shows the power reflection measurements of the CMA and commercial UHF disc sensors used in [33]. The CMA has ultrawide bandwidth compared to the commercial disc sensor. The −10 dB and −6 dB bandwidths of the CMA span over 0.5 to 6.8 GHz and 0.42 to 9.38 GHz, respectively. The CMA has positive gain over 1 to 1.5 GHz with peak gain of 1.8 dB at 1 GHz. The simulated effective height indicated mean value of 19.5 mm in the operating BW (Fig. 2(c)). The peak-to-peak voltage V_{pp} of PD induced UHF signals gathered by the CMA and commercial disc sensors for defects in SF_6 gas filled GIS test cells indicated nearly two-fold increase in the induced voltage for the UHF CMA. The CMA has the largest fractional bandwidth when compared to the spiral [23], [34], [35], slot [21], disc [22], fractal [36] and patch type [37] UHF sensors reported for PD detection. A detailed design and performance comparison of the CMA

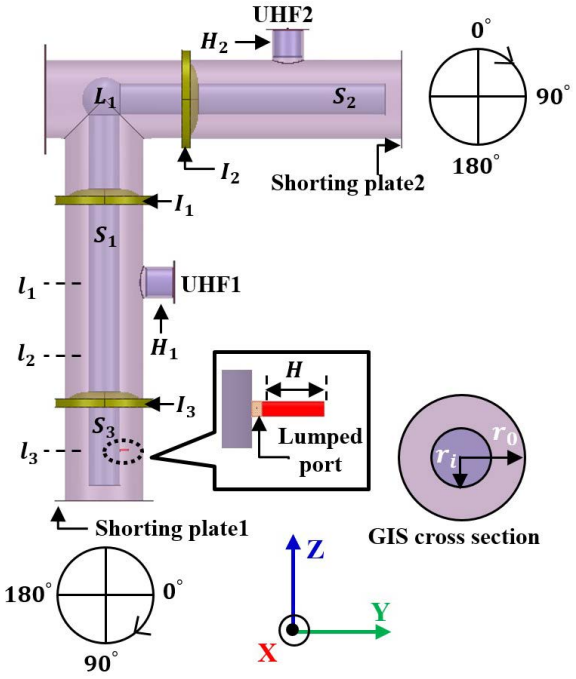

FIGURE 1. A 3 m long L-GIS with shorting plates, handholes, insulating spacers, busbar with disconnector and two internal UHF CMA. GIS inner and outer conductor radii are 60 and 200 mm, respectively. A protrusion defect is modelled as a monopole antenna as shown in the inset.

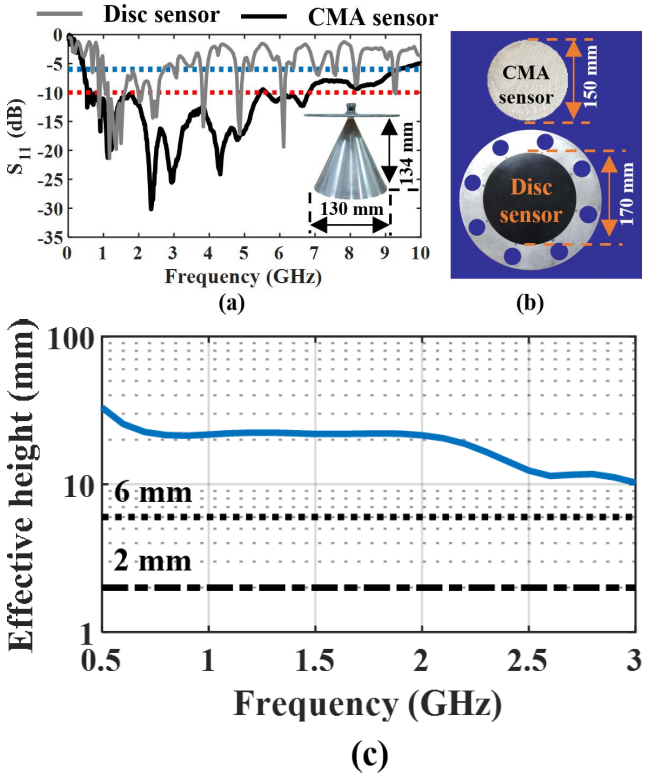

FIGURE 2. (a) Power reflection coefficient of CMA and commercial disc sensor; CMA without radome is shown in inset. (b) Top view of 150 mm diameter CMA with radome and 170 mm diameter disc UHF sensors. (c) Simulated effective height of CMA PD sensor.

with commercial and existing UHF PD sensors can be found in [25].

Three-dimensional (3D) model of the 150 mm diameter UHF CMA with 3D printed dielectric radome and metal cavity was positioned inside handholes H_1 and H_2 located before and after the L bend as shown in Fig. 1. The inner diameter of the hand holes is 160 mm. The sensors were placed perpendicular to the longitudinal axis of the GIS as they will be sensitive to TEM and the higher order TE and TM modes for this arrangement [27]. The two shorting plates placed at the ends of L-GIS confined the EM waves to the GIS.

C. PD DEFECT MODELS

A protrusion defect was modelled as an electrically small monopole antenna of length H and diameter 2 mm at the edge near the inner conductor of straight section S_3. The defect was excited using lumped port in HFSS as shown in Fig. 1. Modal excitation was used for frequency domain analysis and short duration PD pulse was used for time domain analysis. PD source was modelled as Gaussian pulse (GP) and differentiated Gaussian pulse (DGP) using Eqns. (1) and (2), respectively [10]. In Eqns. (1)-(2), a and b denote pulse center and pulse width, respectively.

$$GP(t) = \frac{1}{\sqrt{2\pi b^2}} exp\left(-(t-a)^2 \Big/ 2b^2\right) \quad (1)$$

$$DGP(t) = \left(-(t-a) \Big/ b^2\right) GP(t) \quad (2)$$

Figs. 3(a)-(b) show the time and frequency domains of a DGP with 200 ps pulse width, 2 V V_{pp} and 0.9 ns rise time. As different internal defects generate UHF signals with varying frequency content [33], $GP(t)$ with rise time t_r varying over 0.1–5 ns was used for defect excitation in time domain. Figs. 3(c)-(d) show the time and frequency domains of the zero mean GP for varying rise time t_r. The spectral content of the GP increased from 0.5 to 6.8 GHz as t_r was reduced from 1.32 to 0.12 ns thereby covering the operating bandwidth of the UHF CMA. Numerical modelling using artificial pulses is a convenient tool to understand PD signal characteristics and assess UHF sensor performance. PD defect models used in this study has spectral content in UHF regime and is well accepted in HV community for preliminary evaluation of UHF sensors [11], [32]. The use of artificial voltage pulse from an external function generator is also suggested in CIGRE sensitivity verification test method [19], [38].

D. EM MODES IN GIS

Though GIS is not a perfect coaxial transmission, it supports fundamental TEM mode, and several higher order TE and TM modes as reported in [11], [12], [13], [14], [15], [16], [17], [18], [20], [31], [39], and [40]. Fig. 4 shows the electric field distribution and cut off frequency of the fundamental and first 14 modes calculated for the SF_6 gas filled GIS bus bar modelled in Fig. 1. It can be observed that TEM

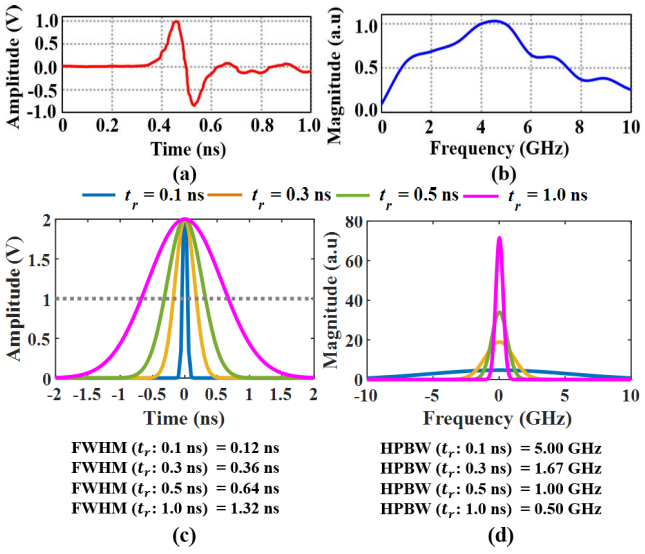

FIGURE 3. Electrical characteristics of PD defect model. (a) Time and (b) frequency domain representations of DGP with 200 ps pulse width, 0.9 ns rise time and 2 V V_{pp}. (c) Time and (d) frequency domain representations of GP for varying rise time.

mode has uniform field distribution along the circumference unlike the higher order TE and TM modes. It can also be observed that TE modes have angular variation in electric field which could influence the signal induced in the UHF sensor depending on sensor orientation and polarization. Furthermore, as the electric field radiated by the PD source is along the radial direction, TE modes are more likely to be excited inside the GIS along with TEM mode when compared to TM modes [27].

In addition to propagation of higher order modes, EM waves undergo attenuation due to conductor and dielectric losses in the GIS [41]. These losses increase with frequency, hence higher order modes attenuate faster than the lower modes [41]. The energy carried by the wave modes decrease exponentially with increase in propagation distance and they propagate with their respective group velocity v_g. The group velocity of TE and TM modes are lower than the velocity of the TEM mode [41], as a result lower order modes travel faster than the higher order modes. Thus, UHF signal propagation inside the GIS is complex due to losses, attenuation and dispersion which affect signal arrival time, shape, amplitude, and spectral content.

E. EM SIMULATIONS

The 3D model of L-GIS in Fig. 1 was analyzed in Ansys HFSS® simulation software. The inner and outer conductors, shorting plates and handholes were assigned as perfect electric conductor, and the basin type spacers I_1, I_2 and I_3 were assigned dielectric constant of 4.4 [39]. The SF_6 gas inside the GIS was assigned dielectric constant of 1.00205 [27]. The 3D model of the UHF CMA was imported in the L-GIS model and positioned in the hand holes to calculate the voltage induced by the protrusion defect. Material properties reported in our earlier work were assigned to the subdomains of the CMA [25]. The internal defect was modelled as a monopole antenna with gap feed. The L-GIS model was placed in an airbox which was terminated by absorbing boundary condition on its external surface to absorb the outward radiated EM waves leaked from the insulating spacers S_1, S_2, and S_3. EM field distribution inside the GIS was calculated by solving 3D vector wave equations. The voltages induced at the wave port terminations of CMA i.e., UHF1 and UHF2 were analyzed in time and frequency domains. The driven modal solver in HFSS was used for frequency domain analysis, and transient solver was used for time domain analysis. Simulations were carried out on a computer (Intel® Xeon® processor E5-1650 v4) with 6 cores and 256 GB random access memory.

F. TEST CASES

A protrusion defect of length $H = 10$ mm placed at l_3 shown in Fig. 1 for 0° orientation with respect to UHF1 and UHF2 was fed with GP excitation. The rise time of the GP was varied over 0.1–10 ns to cover the frequency range of UHF signals reported for internal defects in GIS [12], [39], [40], [41], [42]. The length of the protrusion defect was varied from 10 to 30 mm in steps of 5 mm by keeping the PD source at the farthest location l_3 from the UHF sensors for 0° orientation between the PD source and UHF sensors to study UHF signal attenuation, dispersion and mode propagation inside the L-GIS, influence of defect size on PD induced sensor voltages and the minimum detectable defect size by the UHF sensors.

The location of the protrusion defect was changed to l_1, l_2 and l_3 positions shown in Fig. 1 to study the influence of handhole, spacer and shorting plate, respectively on the UHF signals induced at UHF1 and UHF2. The orientation of the defect and internal UHF sensors was set as 0°. Defect location l_1 is the closest to UHF1 and it is 1100 mm away from shorting plate1. Defect location l_2 is 300 mm away from l_1, and both (l_1, l_2) are located in between the insulating spacers I_1 and I_3. Defect location l_3 which is 550 mm away from l_1 was selected to study the influence of spacer and shorting plate1.

As higher order EM modes have radial and circumferential variations in electric field (Fig. 4), simulations were carried out to assess the influence of source orientation inside the GIS relative to the UHF sensors. Simulations were carried out for a 10 mm long defect at l_3 and source orientations of 0, 90, and 180° relative to the UHF sensors to determine the ability of the CMA to detect PD source positioned at varying angular orientations in the L-GIS.

III. EXTERIMENTAL VERIFICATION

A. EXPERIMENTAL SETUP

Fig. 5(a) shows the laboratory model of the L-GIS with shorting plates 1 and 2, straight sections S_1, S_2 and S_3, and a 90° L section as shown in Fig. 1. The basin type insulating spacers I_1, I_2 and I_3 were made of Nylon using precision

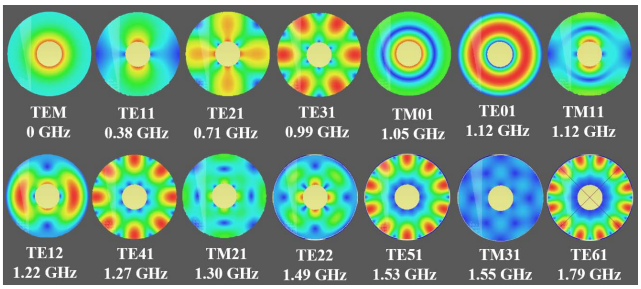

FIGURE 4. Electric field distribution and cutoff frequency for the fundamental and first 14 modes in a coaxial waveguide with inner and outer conductor dimensions same as the SF_6 gas filled 252 kV GIS bus bar.

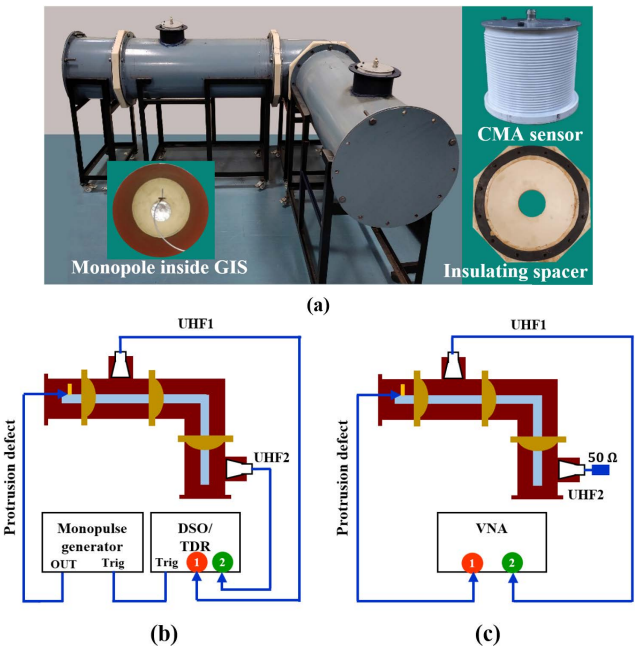

FIGURE 5. UHF sensor measurement setup in L-GIS. (a) L-GIS model, (b) illustrations of time and (c) frequency domain experimental setups.

computer numerical control machining process. The dimensions and locations of the inner and outer conductors, shorting plates, insulating spacers, hand holes and internal UHF1 and UHF2 sensors in Fig. 5(a) are as per the 3D model used in the simulations. Two UHF CMAs were inserted in hand holes H_1 and H_2 and secured to the metal encapsulation using nuts and bolts. UHF sensor measurements inside the L section with geometrical and material discontinuities like a HV L-GIS were gathered using an internal monopole transmitter injecting PD-like signals. A subminiature version A (SMA) connector with an extended inner conductor placed on the inner conductor of the GIS was used to simulate the protrusion defect. The electrically short monopole antenna was connected to an external UHF signal source using low loss coaxial cable. The CMAs at UHF1 and UHF2 were connected to the signal measurement setup using identical low loss coaxial cables.

B. TIME DOMAIN MEASUREMENTS

Fig. 5(b) illustrates the time domain measurement setup. A monopulse generator (AVE2-C-5000, Avtech Electrosystems Ltd., Canada) was used to generate the DGP signal with 2 V V_{pp}, 200 ps pulse width and 0.9 ns rise time. The DGP was fed to the monopole antenna to radiate a short duration PD-like pulse. CMA inside the hand holes were connected to the oscilloscope (DCA-X-86100D, Keysight Technologies, USA). The oscilloscope and pulse generator were synchronized using the trigger output on the pulse generator to simultaneously acquire the voltage induced in the CMA at UHF1 and UHF2. Time domain measurements were acquired for monopole length of 10 to 30 mm for the farthest location l_3, and 0° source orientation with the UHF sensors. Measurements were repeated for 10 mm monopole at l_1, l_2 and l_3 locations for 0° orientation between the source and UHF sensors. UHF sensor measurements were repeated for 90 and 180° relative angle between the source and UHF sensor as in the simulations.

C. FREQUENCY DOMAIN MEASUREMENTS

Fig. 5(c) shows the frequency domain measurement setup. Frequency domain measurements were carried out using a two-port vector network analyzer (VNA) from Keysight Technologies, USA (Model E5071C). Port 1 of the VNA was connected to the monopole antenna i.e., internal defect and port 2 was connected to one of the two UHF sensors. Signal attenuation in the low loss coaxial cables connected to the UHF sensor and internal PD defect was calibrated using VNA. The UHF sensor that was not connected to the VNA was terminated with a 50 Ω load. As the rise time t_r of a trapezoidal pulse is inversely proportional to its bandwidth ($BW = 0.35/t_r$), the frequency sweep in port 1 of the VNA was controlled to vary signal rise time over 0.1 – 10 ns. The VNA start frequency and output power were set as 300 kHz and −10 dBm, respectively. The voltage transmission coefficients between the monopole and UHF sensors UHF1 (S_{21}) and UHF2 (S_{31}) were measured for varying locations and lengths of the monopole antenna, orientations of the UHF sensors with respect to the monopole antenna, and excitation signal BW. Frequency domain measurements were used to understand EM wave attenuation and mode formation inside the GIS before and after the L bend. Frequency domain transmission measurements for varying signal bandwidth were windowed, filtered and converted to time domain for time domain analysis [26], [39].

IV. RESULTS AND DISCUSSION

A. EFFECT OF RISE TIME

Fig. 6 shows the electric field distribution in L-GIS at 3.7 ns for GP excitation. Simulations are shown for defect length, location, and orientation of 10 mm, l_3, and 0°, respectively. Multiple internal reflections observed inside L-GIS in Fig. 6 due to internal discontinuities induced higher order TE and TM modes. The lower order wave modes travel faster

than the higher modes, and spectral strength is higher at lower frequencies for GP with smaller t_r (Fig. 3(d)). Thus, EM waves induced by the PD source reached UHF1 relatively faster with higher amplitude for smaller t_r as observed in Fig. 6. Thus, increase in signal amplitude at UHF1 is not due to increase in the PD signal strength but due to the decrease in signal rise time i.e., increase in spectral content.

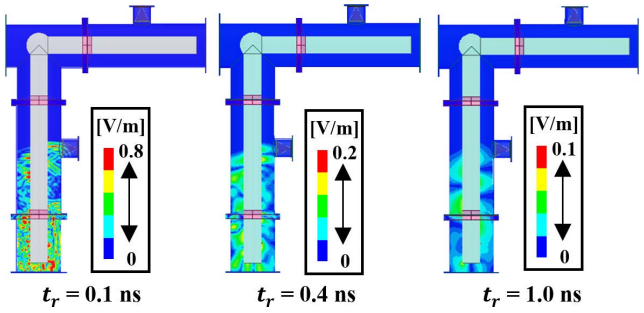

FIGURE 6. Electric field distribution at 3.7 ns inside L-GIS for GP source. Defect length, location, and orientation are 10 mm, l_3, and 0°, respectively.

Fig. 7 shows the voltage induced at UHF1 and UHF2 for GP source with same rise time as in Fig. 6. It can be observed that the UHF signal arrival time for a given UHF sensor is relatively faster for GP with smaller t_r in agreement with the observations in Fig. 6. The time domain measurements of CMA are in good agreement with the simulations and demonstrate the ability of CMA to gather EM waves propagated through the L-GIS. The arrival time of the EM wave in measurements and simulations is relatively longer for UHF2 than UHF1 due to the increase in wave propagation distance from the source. The signal amplitude is weaker for UHF2 due to wave attenuation caused by dielectric and conductor losses, and discontinuities in the propagation path. As wave undergoes attenuation, dispersion, and multipath propagation, EM waves incident on the UHF sensors have longer duration than the pulse width of the GP excitation [29], [43].

Fig. 8 shows the comparison between the peak-peak amplitude of measured and simulated UHF signals for varying rise times. It can be observed that the peak-peak amplitude of UHF1 and UHF2 sensors decreased exponentially with increase in t_r, which agrees with the observations in Figs. 6 and 7. UHF signal amplitude in measurements is lower than the simulations due to dielectric and conductor losses in the fabricated L-GIS. For $t_r = 1.0$ ns, HPBW of the GP is 0.5 GHz, and TEM mode carries most of the energy compared to TE11 (Fig. 3). Further, EM field strength is weak for $t_r \geq 1.0$ ns as superimposition of TEM and TE11 modes is relatively weak.

Fig. 9 shows the scalogram of CMA measurements at UHF1 shown in Fig. 7. It can be observed that the frequency content changes with time, and as time progresses i.e., increase in path length, frequency content in the UHF measurements decreased. This is because, attenuation of higher order modes is more than the lower order modes. This can be clearly noticed in the scalograms of UHF signals for GP excitations with rise time 0.1 and 0.4 ns for which EM wave propagation is due to several higher order modes including TEM mode. For $t_r \geq 1$ ns, frequency content in the scalogram spans 0.3 to 1 GHz indicating that EM wave propagation is due to TEM and the lower order TE11, TE21 and TE31 modes (Fig. 4). Similar signal behavior was observed for UHF2 signals but the signal magnitude is lower than UHF1 as observed in Figs. 7 and 8. From the time and frequency domain analysis, it is concluded that the signal energy in spectral domain decreased with increase in rise time which led to the reduction in UHF signal amplitude with increase in rise time.

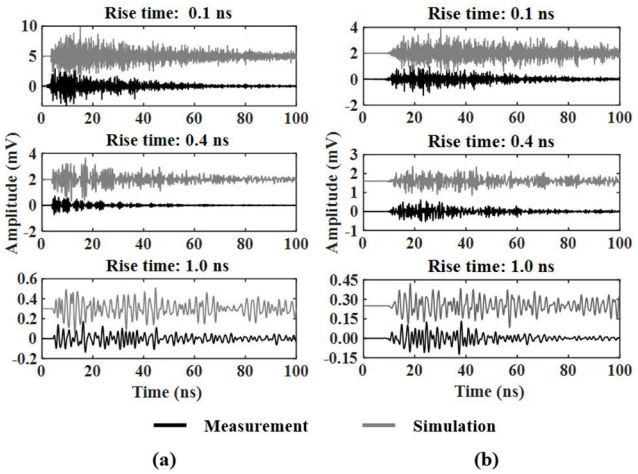

FIGURE 7. Voltage induced in (a) UHF1 and (b) UHF2 sensors for GP excitation of PD defect. Defect length, location, and orientation are 10 mm, l_3, and 0°, respectively.

Simulations and measurements confirm that increase in PD induced UHF signal amplitude is not necessarily due to increase in PD signal magnitude at the inception voltage, but it could also be due to the low rise time of the PD. In [25], we observed the lowest t_r for UHF signals induced by particle movement type of PD defect in SF_6 filled GIS test cell. We also observed that UHF signal t_r for Corona discharge was higher than surface discharge. The amplitude of PD induced UHF signals measured at the respective inception voltages for three PD defects in GIS test cells indicated decrease in signal amplitude with increase in UHF signal rise time. The UHF signal measurements for GP excitation with varying rise times reported here are in agreement with the observations in [25].

B. EFFECT OF DEFECT SIZE

Fig. 10 shows the simulated electric field distribution at 0.2 and 3 GHz due to protrusion PD source excited at l_3 with 10, 20, and 30 mm length for 0° source orientation relative to the UHF sensors. Electric field distribution at 0.2 GHz is TEM mode throughout the L bend for all defect lengths as higher mode propagation starts only from 0.37 GHz (Fig. 4). At 3 GHz, several higher order modes exist, and as a result,

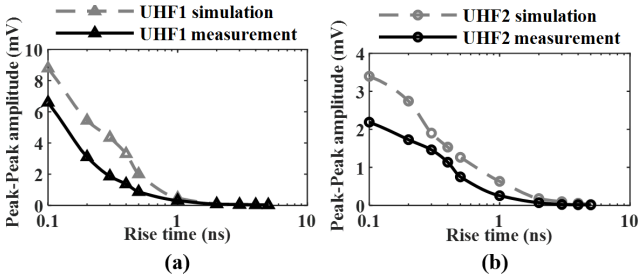

FIGURE 8. Peak-peak amplitude of the voltage induced in (a) UHF1 and (b) UHF2 sensors for GP excitation of PD defect with varying rise time. Defect length, location, and orientation are 10 mm, l_3, and 0°, respectively.

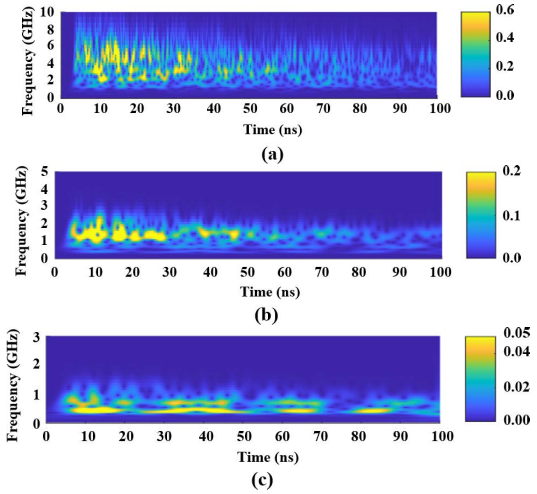

FIGURE 9. Time-frequency analysis of CMA measurements at UHF1 for Gaussian pulse excitation with (a) 0.1 ns, (b) 0.4 ns and (c) 1.0 ns rise time. Defect length, location, and orientation are 10 mm, l_3, and 0°, respectively.

field distribution is complex. The electric field distribution before L bend is predominantly due to the TEM mode and higher order TE modes, whereas TM modes with longitudinal field components contribute after L bend. Electric field distribution remained the same except for an increase in the field intensity with increase in defect size.

Fig. 11 shows the signal transmission loss measured between the protrusion defect at l_3 and UHF sensors ($|S_{21}|^2$, $|S_{31}|^2$) for varying protrusion lengths and 0° source orientation. The signal received by the UHF sensors is the highest for 30 mm protrusion length. It is observed that the signal strength increased with increase in protrusion length at all frequencies. As the protrusion length increased, gap between the PD source and GIS outer conductor decreased, which in turn increased the strength of the internal reflections. The strong reflected waves and forward propagating waves superimposed and increased the EM signal strength received by UHF sensors for increasing defect length. The signal received by UHF2 located after L bend is about 10 dB below UHF1 for all protrusion lengths due to propagation distance, higher order modes, and attenuation and dispersion of the forward propagating wave. The multiple resonances in

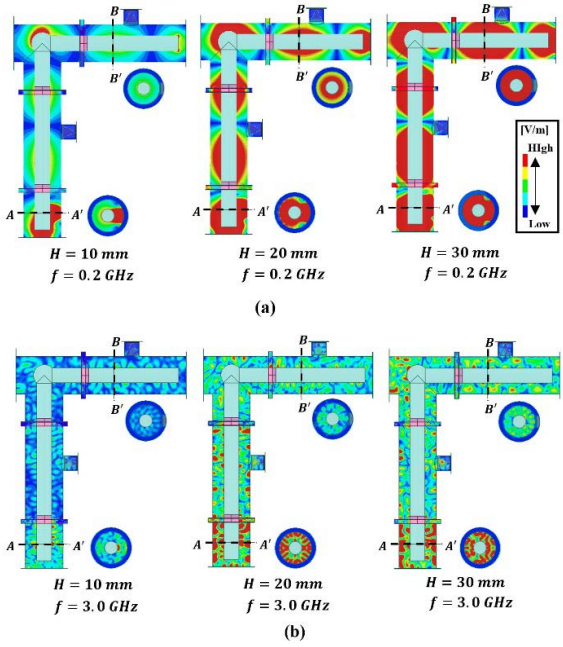

FIGURE 10. Electric field distribution at (a) 0.2 and (b) 3 GHz inside L-GIS for varying lengths of protrusion defect at l_3 and 0° defect orientation.

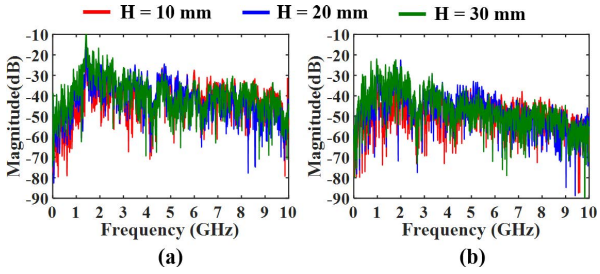

FIGURE 11. Voltage transmission coefficient measured between PD source and UHF CMA at (a) UHF1 and (b) UHF2 for varying lengths of protrusion defect at l_3 and 0° defect orientation.

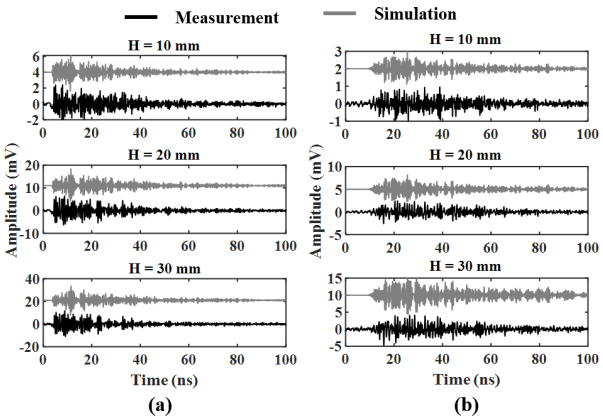

FIGURE 12. Voltage induced in CMA at (a) UHF1 and (b) UHF2 for DGP at l_3 and 0° source orientation with the CMA and varying defect lengths.

Fig. 11 are due to wave reflections and attenuation inside the L-GIS and were also observed in [39].

Fig. 12 shows UHF1 and UHF2 signals for protrusion defect of 10, 20, and 30 mm lengths at l_3 with 0° orientation

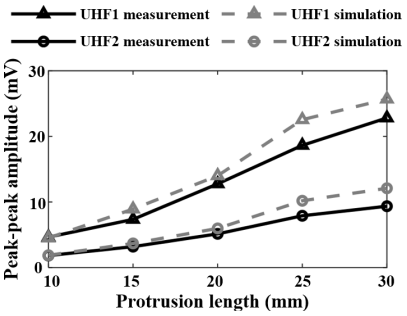

FIGURE 13. Peak-peak amplitude of UHF CMA at UHF1 and UHF2 locations for DGP at l_3, 0° source orientation with the CMA and varying defect lengths.

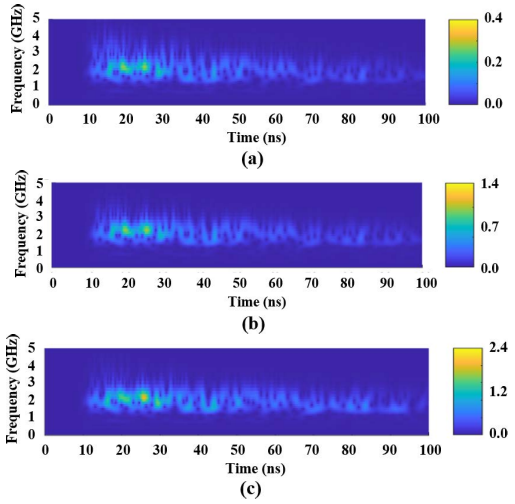

FIGURE 14. Time-frequency analysis of CMA measurements at UHF2 for protrusion defect of (a) 10, (b) 20 and (c) 30 mm lengths excited with DGP at l_3 and 0° orientation with the CMA.

between the PD defect and UHF sensors gathered for DGP excitation. The peak-to-peak amplitude of UHF signals gathered by CMA at UHF1 and UHF2 in Fig. 13 were determined from Fig. 12. Fig. 13 indicates that the induced voltage decreased with increase in protrusion length. As expected, UHF sensor amplitude at UHF2 is weaker than at UHF1. The scalograms of CMA measurements at UHF2 in Fig. 14 clearly shows that the frequency content of UHF signal is independent of protrusion length, and its spectral energy increases with increase in defect length. Time-frequency analysis agrees with the steady state measurements in Figs. 11. It also indicates that the spectral content of UHF signal reduced with increase in observation time due to wave attenuation.

C. EFFECT OF DEFECT LOCATION

Fig. 15(a) shows the peak-peak amplitude of the voltage induced in CMA at UHF1 and UHF2 for DGP excitation of 10 mm protrusion defect at locations l_1, l_2 and l_3, and 0° orientation between the source and UHF sensors. The peak-peak amplitude decreased with increase in the source distance from the UHF sensor. The frequency domain transmission coefficient in Fig. 16 for three source locations also

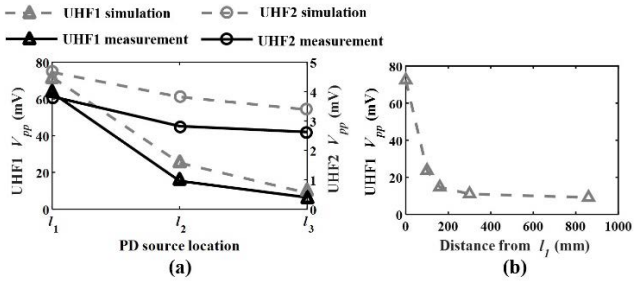

FIGURE 15. Peak-peak amplitude V_{pp} of UHF signals induced in CMA at (a) UHF1 and UHF2 for DGP excitation of 10 mm protrusion defect and 0° e orientation with the sensors at varying defect locations. (b) Simulated V_{pp} at UHF1 for varying defect locations away from l_1 towards l_2.

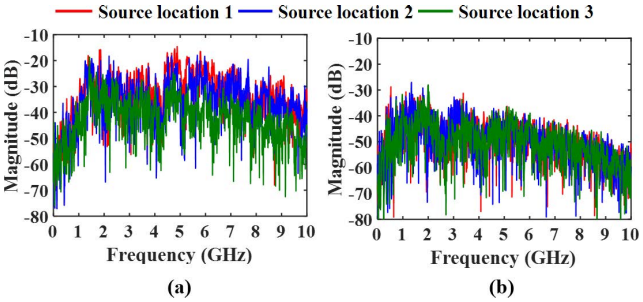

FIGURE 16. Voltage transmission coefficient for varying locations of 10 mm protrusion defect and 0° defect orientation. CMA measurements at (a) UHF1 and (b) UHF2.

TABLE 1. Time domain UHF signal parameters for varying orientations between UHF CMA and PD source of 10 mm length at l_3.

Parameter	UHF1 arrival times (ns)			UHF2 arrival times (ns)		
Sensor Rotation	0°	90°	180°	0°	90°	180°
Simulated	3.6	3.8	4.2	10.4	10.9	11.9
Measured	3.7	4.1	4.3	10.8	11.5	12.4

indicates the highest attenuation for defect at l_3. As EM wave attenuates exponentially along the propagation path, reduction in signal amplitude is larger between source locations l_1 and l_2 when compared to the voltage reduction observed between l_2 and l_3. This is clear from V_{pp} at UHF1 shown in Fig. 15(b) for simulated DGP excitation of the 10 mm defect at varying defect locations away from l_1 moving towards l_2. It can be observed that reduction in signal amplitude due to the spacer is very less as reported in [17] and [20]. Despite the complex wave behavior, signal arrival time at the UHF sensors increased with increase in defect location from the sensors due to propagation length without significantly affecting the spectral amplitude. These observations agree with the studies conducted by Hikita et al. [17], [20] and Wang et al. [27], [28]. Their study also concluded that spacers do not significantly attenuate the UHF signals.

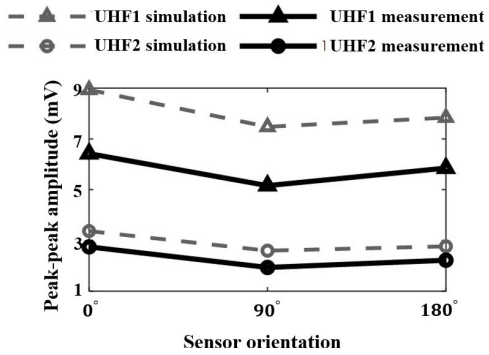

FIGURE 17. Peak-peak amplitude of CMA at UHF1 and UHF2 for 0, 90 and 180° orientations of PD source relative to the 10 mm protrusion defect at l_3.

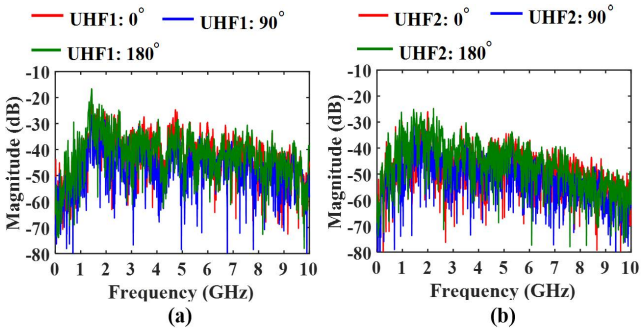

FIGURE 18. Voltage transmission coefficient for varying orientations of the 10 mm protrusion defect and 0° defect orientation. CMA measurements at (a) UHF1 and (b) UHF2.

D. EFFECT OF DEFECT ORIENTATION

Fig. 17 shows the peak-peak amplitude of CMA at UHF1 and UHF2 for 0, 90 and 180° relative angles between the PD source and UHF sensors for DGP excitation of 10 mm long monopole. The corresponding voltage transmission coefficients in Fig. 18 exhibits a change in the spectral magnitude without affecting the spectral content. The arrival times of the UHF signals in Table 1 show small variations for varying angular orientations of the source due to the relatively small change in path length. The signal amplitude is weaker for 90° orientation of the sensor relative to the PD defect as the electric field distribution is perturbed due to the propagation of odd number of TE modes for 90° source orientation [27] [31]. Furthermore, as CMA is linearly polarized, its sensitivity to the incident EM waves also decreased for 90° orientation. UHF2 signals in Figs. 17 and 18 are weaker than UHF1 due to the attenuation of TE modes after L bend (refer 10 mm defect in Fig. 10). Similar observations were also reported for varying orientations of the UHF sensor with respect to the PD source [27], [29], [44].

V. CONCLUSION

A detailed study was carried out to understand the influence of PD defect parameters on the propagation characteristics of EM waves induced in a GIS section. A GIS model with three basin type insulating spacers, hand holes, L bend and bus bar with a disconnector was considered in this work. Small structural details inside the GIS that are also likely to influence the PD induced UHF signals and wave propagation inside GIS were not considered for numerical and experimental simplicity. Though the PD source is modelled as a short monopole, the defect signal models used in this study are widely used for preliminary assessment and sensitivity verification of PD sensor. The characteristics of the PD induced EM signals were analyzed using a linearly polarized UHF CMA. Though the UHF antenna is linearly polarized, near field measurements in the simplified L-GIS laboratory setup with electrically large internal structures gathered in the absence of HV indicate the ability to detect EM waves propagated for varying parameters of the PD-like signals. Despite the study limitations on PD source and L-GIS setup, EM wave propagation inside the GIS was explained satisfactorily in time and frequency domains, and provided additional insights on UHF signal propagation inside the GIS and UHF sensor characteristics desirable for internal sensing of PD activity. The outcomes of this study are summarized in the following concluding remarks.

- Increase in UHF signal amplitude is not always due to increase in the intensity of the inception voltage or defect size. The amplitude of UHF signal due to a PD activity with fast rise time will be more than that due to a different PD activity with slow rise time occurring at their respective inception voltage.
- For a PD activity with a given rise time, increase in defect size increases the UHF signal amplitude without affecting the frequency content. The increase in signal strength is not due to the intensity of the inception voltage, but due to the strong reflected signals inside the GIS.
- The amplitude of the UHF signal decreased exponentially with increase in the distance of the UHF sensor from the PD activity. TEM and higher order TE modes alone contribute to UHF signals before L bend, whereas TM modes contribution also exists after L bend.
- The amplitude of PD induced UHF signal is the maximum when PD defect and UHF sensor are in line of sight with 0° orientation. The amplitude is the minimum for 90° orientation due to attenuation of higher order TE modes. The UHF signal strength for 90° orientation could be improved if the UHF sensor is circularly polarized.

Preliminary measurements gathered in a L-GIS setup with geometrical and material discontinuities using an internal transmitter injecting PD-like signals and two internal UHF sensors clearly indicate that EM wave propagation inside the GIS is complex and severely influenced by the PD defect parameters. It is also concluded that the UHF CMA has the sensitivity to detect the changes in UHF signal characteristics. Based on this study outcomes, an experimental study with real PD defects is currently under progress.

REFERENCES

[1] M. D. Judd, Y. Li, and I. B. B. Hunter, "partial discharge monitoring of power transformers using UHF sensors. Part I: sensors and signal interpretation," *IEEE Elect. Insul. Mag.*, vol. 21, no. 2, pp. 5–14, Mar./Apr. 2005.
[2] T. Pinpart and M. D. Judd, "Experimental comparison of UHF sensor types for PD location applications," in *Proc. IEEE Electr. Insul. Conf.*, May 2009, pp. 26–30.
[3] S. Tenbohlen, D. Denissov, S. M. Hoek, and S. M. Markalous, "Partial discharge measurement in the ultra high frequency (UHF) range," *IEEE Trans. Dielectr. Electr. Insul.*, vol. 15, no. 6, pp. 1544–1552, Dec. 2008.
[4] G. Robles, R. Albarracín, and J. L. Vázquez, "Antennas in partial discharge sensing system," in *Handbook Antenna Technologies*, 3rd ed. Berlin, Germany: Springer, 2015, pp. 2419–2474.
[5] *High Voltage Test Techniques: Measurement of Partial Discharge by Electromagnetic and Acoustic Methods*, Standard IEC/TS 62478, International Electrotechnical Commission, Geneva, Switzerland, 2016.
[6] H. Janani, B. Kordi, and M. J. Jozani, "Classification of simultaneous multiple partial discharge sources based on probabilistic interpretation using a two-step logistic regression algorithm," *IEEE Trans. Dielectr. Electr. Insul.*, vol. 24, no. 1, pp. 54–65, Feb. 2017.
[7] M. X. Zhu, J. Y. Xue, J. N. Zhang, Y. Li, J. B. Deng, H. B. Mu, G. J. Zhang, X. J. Shao, and X. W. Liu, "Classification and separation of partial discharge ultra-high-frequency signals in a 252 kV gas insulated substation by using cumulative energy technique," *IET Sci. Meas. Technol.*, vol. 10, no. 4, pp. 316–326, 2016.
[8] M. Wu, H. Cao, J. Cao, H.-L. Nguyen, J. B. Gomes, and S. P. Krishnaswamy, "An overview of state-of-the-art partial discharge analysis techniques for condition monitoring," *IEEE Elect. Insul. Mag.*, vol. 31, no. 6, pp. 22–35, Nov./Dec. 2015.
[9] A. Darwish, S. S. Refaat, H. A. Toliyat, and H. Abu-Rub, "On the electromagnetic wave behavior due to partial discharge in gas insulated switchgears: State-of-art review," *IEEE Access*, vol. 7, pp. 75822–75836, 2019.
[10] Q. Khan, S. S. Refaat, H. Abu-Rub, and H. A. Toliyat, "Partial discharge detection and diagnosis in gas insulated switchgear: State of the art," *IEEE Elect. Insul. Mag.*, vol. 35, no. 4, pp. 16–33, Jul. 2019.
[11] A. Darwish, S. S. Refaat, H. Abu-Rub, and H. A. Toliyat, "PD signal propagation in GIS: Ultra-high frequency detection-based modeling," *IEEE Sensors J.*, vol. 20, no. 16, pp. 9417–9426, Aug. 2020.
[12] S. Okabe, G. Ueta, H. Hama, T. Ito, M. Hikita, and H. Okubo, "New aspects of UHF PD diagnostics on gas-insulated systems," *IEEE Trans. Dielectr. Electr. Insul.*, vol. 21, no. 5, pp. 2245–2258, Oct. 2014.
[13] S. Okabe, H. Muto, M. Yoshimura, C. Nishida, and S. Yuasa, "Simulation of propagation characteristics of higher order mode electromagnetic waves in GIS," *IEEE Trans. Dielectr. Electr. Insul.*, vol. 13, no. 4, pp. 855–861, Aug. 2006.
[14] M. Hikita, S. Ohtsuka, T. Teshima, S. Okabe, and S. Kaneko, "Examination of electromagnetic mode propagation characteristics in straight and L-section GIS model using FD-TD analysis," *IEEE Trans. Dielectr. Electr. Insul.*, vol. 14, no. 6, pp. 1477–1483, Dec. 2007.
[15] S. Kaneko, S. Okabe, M. Yoshimura, H. Muto, C. Nishida, and M. Kamei, "Partial discharge diagnosis method using electromagnetic wave mode transformation in actual GIS structure," *IEEE Trans. Dielectr. Electr. Insul.*, vol. 15, no. 5, pp. 1329–1339, Oct. 2008.
[16] T. Hoshino, S. Maruyama, and T. Sakakibara, "Simulation of propagating electromagnetic wave due to partial discharge in GIS using FDTD," *IEEE Trans. Power Del.*, vol. 24, no. 1, pp. 153–159, Jan. 2009.
[17] M. Hikita, S. Ohtsuka, G. Ueta, S. Okabe, T. Hoshino, and S. Maruyama, "Influence of insulating spacer type on propagation properties of PD-induced electromagnetic wave in GIS," *IEEE Trans. Dielectr. Electr. Insul.*, vol. 17, no. 5, pp. 1642–1648, Oct. 2010.
[18] S. Okabe, S. Kaneko, M. Yoshimura, H. Muto, C. Nishida, and M. Kamei, "Partial discharge diagnosis method using electromagnetic wave mode transformation in gas insulated switchgear," *IEEE Trans. Dielectr. Electr. Insul.*, vol. 14, no. 3, pp. 702–709, Jun. 2007.
[19] A. Darwish, G. Coapes, S. S. Refaat, H. Abu-Rub, and H. A. Toliyat, "PD signal attenuation in 550-kV GIS: Impact of different barriers on the propagation of electromagnetic waves," *IEEE Trans. Instrum. Meas.*, vol. 70, pp. 1–13, 2021.
[20] M. Sawada, K. Omori, S. Isejima, S. Ohtsuka, H. Ikeda, M. Hikita, G. Ueta, S. Okabe, T. Hoshino, S. Maruyama, and T. Sakakibara, "Influence of metal flange cover of insulation spacers on propagation properties of PD-induced electromagnetic wave in GIS," in *Proc. Int. Conf. Condition Monitor. Diagnosis*, Beijing, China, 2008, pp. 437–442.
[21] C. Zachariades, R. Shuttleworth, and R. Giussani, "A dual-slot barrier sensor for partial discharge detection in gas-insulated equipment," *IEEE Sensors J.*, vol. 20, no. 2, pp. 860–867, Jan. 2020.
[22] Z. Huamao, L. Yazhou, and Z. Shusheng, "Study on the disc sensor based on the cavity mold theory," *IEEE Sensors J.*, vol. 16, no. 13, pp. 5277–5282, Jul. 2016.
[23] S. Park and K. Y. Jung, "Design of a circularly-polarized UHF antenna for partial discharge detection," *IEEE Access*, vol. 8, pp. 81644–81650, 2020.
[24] C. Zachariades, R. Shuttleworth, R. Giussani, and T.-H. Loh, "A wideband spiral UHF coupler with tuning nodules for partial discharge detection," *IEEE Trans. Power Del.*, vol. 34, no. 4, pp. 1300–1308, Aug. 2019.
[25] Y. R. Yadam, S. Ramanujam, and K. Arunachalam, "An ultrawideband conical monopole with radome for detection of partial discharges," *IEEE Sensors J.*, vol. 21, no. 17, pp. 18764–18772, Sep. 2021.
[26] Y. R. Yadam, B. T. Sivaprakasam, K. C. Venkata, and K. Arunachalam, "Step frequency continuous wave RADAR sensor for level measurement of molten solids," *J. Electromagn. Waves Appl.*, vol. 32, no. 3, pp. 281–292, 2018.
[27] T. Li, X. Wang, C. Zheng, D. Liu, and M. Rong, "Investigation on the placement effect of UHF sensor and propagation characteristics of PD-induced electromagnetic wave in GIS based on FDTD method," *IEEE Trans. Dielectr. Electr. Insul.*, vol. 21, no. 3, pp. 1015–1025, Jun. 2014.
[28] X. Wang, T. Li, D. Ding, and M. Rong, "The influence of L-shaped structure on partial discharge radiated electromagnetic wave propagation in GIS," *IEEE Trans. Plasma Sci.*, vol. 42, no. 10, pp. 2536–2537, Oct. 2014.
[29] T. Li, M. Rong, X. Wang, and J. Pan, "Experimental investigation on propagation characteristics of PD radiated UHF signal in actual 252 kV GIS," *Energies*, vol. 10, no. 7, p. 942, Jul. 2017.
[30] W. Gao, D. Ding, W. Liu, and X. Huang, "Propagation attenuation properties of partial discharge in typical in-field GIS structures," *IEEE Trans. Power Del.*, vol. 28, no. 4, pp. 2540–2549, Oct. 2013.
[31] T. Li, M. Rong, D. Liu, and X. Wang, "Study on propagation characteristics of partial discharge-induced UHF signal in GIS with l shaped structure," in *Proc. 2nd Int. Conf. Electric Power Equip.-Switching Technol. (ICEPE-ST)*, Oct. 2013, pp. 1–4.
[32] T. Zhao, M. D. Judd, and B. G. Stewart, "Simulation study on the effect of PD pulse shape on electromagnetic wave propagation in an L-type GIS structure," in *Proc. IEEE Electr. Insul. Conf. (EIC)*, Jun. 2021, pp. 686–689.
[33] R. Umamaheswari and R. Sarathi, "Identification of partial discharges in gas-insulated switchgear by ultra-high-frequency technique and classification by adopting multi-class support vector machines," *Electr. Power Compon. Syst.*, vol. 39, no. 14, pp. 1577–1595, 2011.
[34] W. Zhou, P. Wang, Z. Zhao, Q. Wu, and A. Cavallini, "Design of an archimedes spiral antenna for PD tests under repetitive impulsive voltages with fast rise times," *IEEE Trans. Dielectr. Electr. Insul.*, vol. 26, no. 2, pp. 423–430, Apr. 2019.
[35] P. Wang, S. Ma, S. Akram, K. Zhou, Y. Chen, and M. T. Nazir, "Design of archimedes spiral antenna to optimize for partial discharge detection of inverter fed motor insulation," *IEEE Access*, vol. 8, pp. 193202–193213, 2020.
[36] M. M. O. Harbaji, A. H. Zahed, S. A. Habboub, M. A. AlMajidi, M. J. Assaf, A. H. El-Hag, and N. N. Qaddoumi, "Design of Hilbert fractal antenna for partial discharge classification in oil-paper insulated system," *IEEE Sensors J.*, vol. 17, no. 4, pp. 1037–1045, Feb. 2017.
[37] G. V. R. Xavier, E. G. Da Costa, A. J. R. Serres, L. A. M. M. Nobrega, A. C. Oliveira, and H. F. S. Sousa, "Design and application of a circular printed monopole antenna in partial discharge detection," *IEEE Sensors J.*, vol. 19, no. 10, pp. 3718–3725, May 2019.
[38] U. Schichler, W. Koltunowicz, D. Gautschi, A. Girodet, H. Hama, K. Juhre, J. Lopez-Roldan, S. Okabe, S. Neuhold, C. Neumann, and J. Pearson, "UHF partial discharge detection system for GIS: Application guide for sensitivity verification," in *Proc. VDE High Voltage Technol. ETG-Symp.*, 2016, pp. 1–9.
[39] G. Behrmann, K. Wyss, J. Weiss, M. Schraudolph, S. Neuhold, and J. Smajic, "Signal delay effects of solid dielectrics on time-of-flight measurements in GIS," *IEEE Trans. Dielectr. Electr. Insul.*, vol. 23, no. 3, pp. 1275–1284, Jun. 2016.
[40] T. Ito, M. Kamei, G. Ueta, and S. Okabe, "Improving the sensitivity verification method of the UHF PD detection technique for GIS," *IEEE Trans. Dielectr. Electr. Insul.*, vol. 18, no. 6, pp. 1847–1853, Dec. 2011.

[41] R. Mishra, H. Muthukrishnan, A. Ramanan, and R. Sarathi, "Understanding partial discharge activity in GIS due to particle movement under high frequency AC voltage adopting UHF technique," in *Proc. 6th Int. Conf. Ind. Inf. Syst.*, Aug. 2011, pp. 93–97.
[42] K. Nishigouchi, M. Kozako, M. Hikita, T. Hoshino, S. Maruyama, and T. Nakajima, "Waveform estimation of particle discharge currents in straight 154 kV GIS using electromagnetic wave propagation simulation," *IEEE Trans. Dielectr. Electr. Insul.*, vol. 20, no. 6, pp. 2239–2245, Dec. 2013.
[43] M. Hikita, S. Ohtsuka, J. Wada, S. Okabe, T. Hoshino, and S. Maruyama, "Propagation properties of PD-induced electromagnetic wave in 66 kV GIS model tank with L branch structure," *IEEE Trans. Dielectr. Electr. Insul.*, vol. 18, no. 5, pp. 1678–1685, Oct. 2011.
[44] T. Li, J. Pan, X. Li, X. Pang, C. Gu, M. Rong, and X. Wang, "The optimal circumferential angle position of UHF sensor for partial discharge detection in GIS," in *Proc. IEEE Int. Conf. High Voltage Eng. Appl. (ICHVE)*, Sep. 2016, pp. 1–4.

YUGANDHARA RAO YADAM received the M.S. degree from the Indian Institute of Technology Madras (IIT Madras), Chennai, India, in 2016, where he is currently pursuing the Ph.D. degree with the Department of Engineering Design, IIT Madras, working on design of UHF sensors and modeling partial discharge signal propagation in GIS.

RAMANUJAM SARATHI (Senior Member, IEEE) received the Ph.D. degree from the Indian Institute of Science, Bengaluru, in 1994. He is currently a Professor and the Head of the High Voltage Laboratory, Department of Electrical Engineering, IIT Madras, Chennai, India. His research interests include condition monitoring of power apparatus and nano materials.

KAVITHA ARUNACHALAM (Senior Member, IEEE) received the Ph.D. degree from Michigan State University, East Lansing, MI, USA, in 2007. She is currently a Professor and the Head of the Electromagnetic Research Laboratory, Department of Engineering Design, IIT Madras, Chennai, India. Her research interests include EM sensors and antennas for nondestructive material measurements, bio-electromagnetics, and EM material characterization.